Speciation in nanosecond laser ablation of zinc in water

Stefan Reich[1,3], Yannis Klügl[1], Anna Ziefuss[2], René Streubel[2], Jörg Göttlicher[1], and Anton Plech[1*]

[1]*Institute for Photon Science and Synchrotron Radiation, Karlsruhe Institute of Technology, Karlsruhe D-76021, Germany;*
[2]*Department of Technical Chemistry I and Center for Nanointegration Duisburg-Essen, University of Duisburg-Essen, Essen D-45141, Germany;*
[3]*Fraunhofer Institute for High-Speed Dynamics, Ernst-Mach-Institute (EMI), Freiburg 79104, Germany*

In situ experimental methods have been applied to resolve mass flow and chemical speciation in the pulsed laser ablation of zinc in water. The chemical speciation has been resolved by time-resolved μ-X-ray absorption spectroscopy and mapped onto the macroscopic mass flow during material ejection from the metallic target and bubble dynamics of evaporated water. Large particles and agglomerates have been detected via dark-field X-ray imaging with a Shack-Hartmann sensor. The characteristic of the dynamics is that the vapor bubble is nearly homogeneously filled with ablated material. This persists during bubble collapse, which means that the ablated particles are captured and retracted towards the target. Limited mass escape is indicated by the X-ray absorption signal. Importantly, the near-edge structure at the Zn-K_α transition delivers information on the chemical state of the ejected material. It clearly confirms that oxidation is not present within the bubble phase and the following sub-millisecond time scale. The oxidation proceeds on Zn nanoparticles in suspension on a second to minute course. Within the first microseconds, a Zn atom phase is detected that resembles Zn vapor. The addition of either reductive $NaBH_4$ or oxidative $HAuCl_4$ to the water phase influences the quantity of the atom contribution moderately, but does not influence the initial atom phase. Such behavior must be understood in terms of the nanosecond pulse excitation. After ejected material and a plasma is formed within the pulse duration of 7 ns the laser is able to further heat the ejecta and transform it partly into vapor. Correspondingly, the coupling of energy into the ablation zone as followed by plasma intensity and bubble size follows a threshold behavior as a function of laser fluence, marking the onset of laser-plasma heating. The reaction conditions inside the bubble are probably reductive due to the concomitant formation of excess hydrogen.

laser ablation in liquids, elemental speciation, X-ray absorption spectroscopy, oxidation, zinc oxide nanoparticles

PACS number(s):   79.20.Eb, 61.46.+w, 87.64.Gb, 81.65.Mq

1 Introduction

Pulsed laser ablation in liquids (PLAL) has been employed for almost 30 years for the synthesis of basic and complex nanoparticles in a green process. From the early work of Fojtik et al. [1] and Neddersen et al. [2], immense progress has been achieved in understanding the process in more detail [3,4] as well as being able to produce chemically-tailored nanoparticles and alloys [5], in particular such of high entropy, defined defect structure and activity [6], not achievable by other methods.

Nevertheless, the majority of information is inferred by theoretical considerations [7-9] or final-state analysis of the ablation products. It remains a challenge to obtain *in situ* information on the structure formation process, in particular on an atomic to particle level, and correlate it to hierarchical processes on the macroscale.

Matsumoto et al. [10, 11] and Lam et al. [12, 13] have employed laser-induced breakdown spectroscopy and vibrational spectroscopy to gain information on early chemical species during material ejection and bubble nucleation. It could be confirmed that dissolved ions are able to enter the bubble vapor to interact with the nascent structures. This was later confirmed by nanoparticle size quenching through such evaporated species [14, 15]. Lam et al. [12] observed hot AlO molecules that show a high temperature within the first few microseconds such that condensation is inhibited. Time-resolved Raman scattering led Takeuchi and Sasaki [16] to conclude that in nanosecond ablation of titanium the particles are metallic at 100 μs, while at 200 μs oxidized particles are present.

General mechanisms have been clarified in recent years, such as the importance of phase explosion of the ablated material together with liquid-film lift-off and jet formation in the melt layer for the inherent polydispersity of the particle product [3, 4, 17]. Differences between ultrashort (few picoseconds) pulse ablation and nanosecond pulse ablation are seen in simulations [9], showing higher importance of heat and spinodal decomposition in nanosecond ablation versus stress confinement and liquid-layer formation and breakup into droplets for ultrashort ablation. While the simulations do not (yet) include laser and plasma interaction with the ejecta, experimental studies have pointed out that the laser-induced plasma can interfere with particle ripening and lead to secondary size reduction [18-21]. A different coarsening mechanism has been identified during the retraction of ejecta inside the bubble towards the target upon bubble collapse. The confinement leads to an agglomeration step that may spoil the particle size definition further [22, 23]. In part, such information was accessible through X-ray small angle scattering [24], specifically identifying nascent nanoparticles. A quantitative mass determination is still challenging, in particular as visible light scattering methods [25] are hampered by the geometry and scattering characteristics.

Earlier, we have demonstrated that X-ray absorption spectroscopy (XAS) in an energy-dispersive mode [26, 27] is able to resolve the absolute mass of a selected element intersected by the X-ray beam as well as providing speciation information on the chemical state. The ablation of zinc by nanosecond laser pulses leads to a large fraction of atomic zinc species inside the cavitation bubble with a life-time of tens of microseconds. The condensation, however, does not lead to immediate oxide formation, although the bubble may contain both oxygen and hydrogen [28, 29]. Oxidation sets in on a second to minute time scale [30].

Within this report, we shed light on the reason for the large atom fraction and the missing oxidation by adding reducing or oxidizing electrolytes to the water phase. Hierarchical processes during PLAL lead to a mutual influence of nanoparticle formation, energy localization, and dissipation including plasma formation, bubble formation, and transport in the liquid medium. The analysis of bubble dynamics and threshold behavior consequently highlights the action of the pulse length on localizing energy at the interaction point.

2   Materials and methods

Ablation setup   The ablation process is performed in a miniature 3D-printed chamber made of UV-curable resin. The access windows consist of an attached 12.5 mm diameter plano-convex lens with the flat side contacting the water for laser access. Its focal length ensures a focusing of the laser pulses onto the rear wall, where a wire target of zinc (1 mm diameter, Chempur, 99.9%) is slowly transported. Probe access is provided by two opposite windows allowing to intersect the laser path and target in a perpendicular direction by the X-ray beam or the pulsed visible light. In the X-ray experiment, two sealed polyimide windows (Kapton, DuPont) contain the water, while for optical videography glass cover slides are used. The deionized water (MilliPore systems) is constantly pumped through the vessel with a gear pump from reservoirs of 20 L, which are frequently refreshed. Part of the X-ray spectroscopy was performed on water containing either 0.3 mM NaBH$_4$ (pH 7.6) or 0.5 mM HAuCl$_4$ (pH 2.6). The run time of these solutions was limited by hydrogen bubbling, respectively formation of gold nanoparticles. Therefore the liquid was exchanged after 3 h. Videography partly used fresh water from a syringe pump.

Laser irradiation and synchronization   The laser irradiation source is a Nd:YAG nanosecond q-switched laser (Minilite I, Continuum) operated at about 1 Hz and 10 mJ (visible) or 12 mJ (X-ray) per pulse at 1064 nm wavelength. Furthermore, a continuous pulse energy variation from 0.3 to 30 mJ is done for visible imaging using the built-in rotating polarizer of the laser. In that case, the energy is calibrated by an energy monitor (PDI-400, Becker&Hickl). The multimode laser beam is focused onto a 70 μm spot (full width at half maximum) on the target, which leads to an ablation crater of about 0.2 mm in diameter. The pulses are synchronized to the synchrotron in a way that one laser trigger induces 200 subsequent detector readouts with 11.4 μs distance

for XAS, 50 readouts for X-ray imaging, or one detector readout for visible imaging. The first 60 frames in XAS are recorded before the laser impact and can be used as background data.

Energy-dispersive X-ray spectroscopy The X-ray spectroscopy is performed at the beamline ID24 at the European Synchrotron Radiation Facility. Briefly, a curved poly-chromator concentrated the X-ray emission from the insertion device into a focus spot of 2.6 μm × 4.2 μm. As the different energies around the zinc K-edge of 9.65 keV converge with a slightly different angle onto the focal spot, the detection on a distant linear detector (Ge microstrip [31]) allows for an energy-resolved detection.

X-ray spectra are taken over a series of heights from 0.07 to 0.37 mm above the target ablation spot with possible lateral shifts. Averaging over adjacent positions and repeated laser pulses was done over about 2000 events for $NaBH_4$ or $HAuCl_4$ or 4000 shots for pure water [27]. Distorted spectra had to be individually discarded (for instance, when intersecting hydrogen bubbles). Time-resolved X-ray spectra are background-subtracted by the spectra before laser irradiation. The regions from 9.5-9.63 and 9.67-9.9 keV are used to remove a linear slope and derive the step height at the Zn-K_α. Near-edge spectra were compared with reference spectra of zinc vapor [32] and zinc metal and ZnO powder [30]. A linear fit of the relative contributions to the measured signal was used as a measure for the relative concentration of these 3 species.

Visible-light stroboscopic imaging and plasma detection A pulsed-laser source is used for illumination (laser diode SPL PL90_3 at 905 nm, Osram; laser driver LDP-V 40-70, Picolas) with collimation optics and is synchronized to the exposure of a digital camera (ace acA1300-60gm, Basler). The light is imaged onto the camera by a photo lens (50 mm, Ernitec). Subsequent images with a shifted delay between laser emission and acquisition are triggered by a delay generator (9424, Quantum Composers), which also defines the pulse length of the laser diode. A short-pass filter at 1000 nm prevents overexposure by the scattered nanosecond laser light. A dichroic beam splitter cube in the imaging path allows extracting the visible-light portion of the image to be focused onto an avalanche detector (APM-400, Becker&Hickl) with 0.44 ns time resolution. The plasma emission signal is recorded on a storage oscilloscope (Wave surfer 500 MHz, LeCroy). Filters (long-pass 550 nm and short-pass 700 nm) exclude the second harmonic from the laser and the illumination light from being recorded. The plasma plume is imaged onto an area larger than the APM sensor. The distance of the shock front, bubble height, and width is extracted from single visible images using the magnification of 3.588 μm per pixel.

X-ray dark-field data analysis Data of X-ray dark-field (Shack-Hartmann) imaging were taken from ref. [27]. Briefly, a mask produces a regular array of X-ray beamlets that intersect the sample and are registered on an area detector to derive absorption, phase shift, and beamlet broadening. The latter is interpreted as a dark-field signal originating from nanoparticles of 25-100 nm in diameter [27,30]. The signal from selected imaged areas is averaged to analyze the amplitude of scattering in the X-ray beam path as a function of delay. It is interpreted as the particle mass in the mentioned sensitivity interval. A model to simulate the temporal change is to assume that either the total mass (from spectroscopy) or the selected nanoparticles are homogeneously dispersed in the bubble and the total amount contained in the bubble is constant in time. Thus, at a low distance from the target maxima in the signals appear whenever the bubble reaches a size comparable to the distance. For a larger bubble, the intersected mass is reduced accordingly.

3 Results and discussion

3.1 Macroscopic dynamics

The interdependence of nanoscopic and macroscopic dynamics during PLAL has been investigated extensively in the past years [33,34]. PLAL on flat target surfaces in a low viscosity liquid, such as water, shows very common behavior on the macroscale. The laser impacts on the surface, causing the material to be heated and ablated. In visible imaging, a strong plasma plume is observed, together with a concentric emission of a shock front that travels at or above the speed of sound. Later, a vapor bubble may be detected to grow to a maximum size and collapse again. Corresponding time-resolved snapshots are shown in Figure 1 together with quantitative observables, such as bubble dynamics, shock front propagation, or detection of the light emission by the ablation plume (Figure 1(a)). This will be discussed in relation to established knowledge.

The bubble is observed on the right side of the image series a) growing from 1.2 to 45 μs. After the collapse, some individual small bubbles are frequently detected (at 2500 μs). We observe that the bubble grows with a power law behavior (same data in the double logarithmic representation of the bubble dimensions in Figure 1(c)), given as 2/5 by Long et al. [35]. We observe a lower aspect ratio $2h/w$ below 1 μs, which then approaches unity as for a hemispherical bubble shape. Earlier experiments have shown that even irradiation of elongated spots on the target may produce hemispherical bubbles due to the dominance of interface tension [20]. Remarkably, bubbles for different excitation conditions and tar-
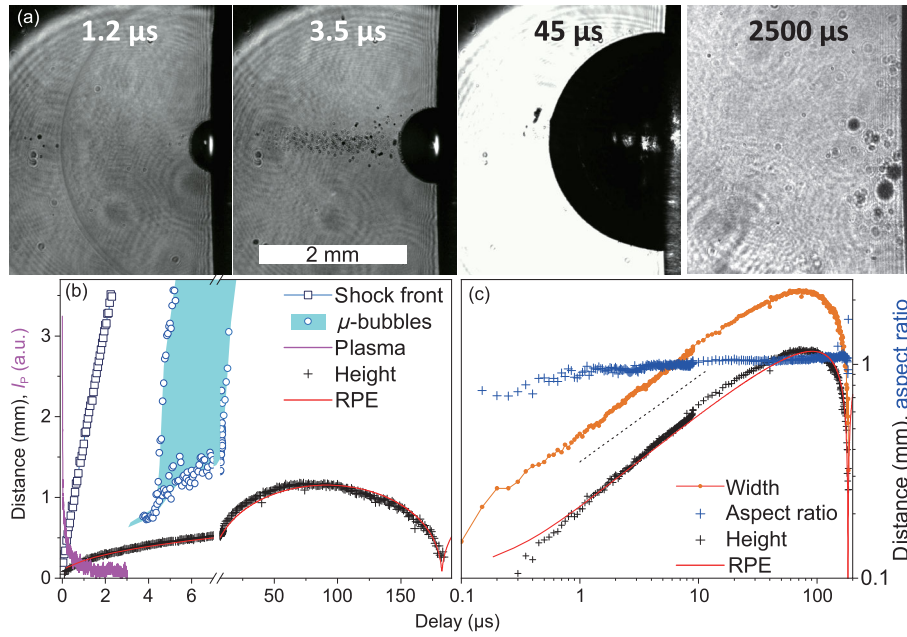
Figure 1   (Color online) (a) Visible-light stroboscopic images at varied delays of 1.2, 3.5, 45, and 2500 μs between laser pulse (10 mJ) and image probe. The scale bar marks 2 mm. The laser beam enters the area from the left at the center of the image, while the target is seen as a black shadow on the right side. The laser diode emission extends over a circular area showing interference fringes. At 1.2 μs, the circular gray ring identifies the shock wave front. At 3.5 μs, the laser-intersected path from the left is populated by a cloud of microbubbles that show a limited extension relative to the distance from the target. (b), (c) Temporal position of the bubble dimensions (height h along the horizontal coordinate and width w along the vertical coordinate along the target surface), shock wave, and limits of the distance of microbubbles from the target. An overlay exemplifies the trace of the plasma emission I_P in arbitrary units and the aspect ratio $2h/w$ of the bubble. The double-logarithmic plot of the same data set in (c) illustrates the power-law behavior of exponent 2/5 at early times (black dashed line) together with a solution of the RPE (solid red line).

get geometries follow very similar behavior, sufficiently well described by the Rayleigh-Plesset equation (RPE) [36]. The symmetry starts to diverge upon bubble retraction and collapse, where effects of the compressible liquid medium [37], vapor condensation, equation of state of the vapor [38] or geometry comes into play [39-41]. The bubble collapse has drawn a lot of attention, because of its relevance for cavitation erosion and material transport. While a symmetric case is set to produce a symmetric collapse, any deviations from symmetry, such as target curvature [42], contact angles (viscous drag), or bubble nucleation away from the surface may cause a wealth of different dynamics, like jet formation [43-45].

Water flow, slightly curved wire target (here 1 mm diameter), and pre-irradiation of the target [46] blur the exact collapse symmetry. Consequently, no jet formation is observed here. Instead, the bubble collapses in a prolate fashion (large aspect ratio), resembling intermediate stages described in refs. [45,47]. The bubble rebound is marked by the flow around the curved surface to experience a lift-off from the surface. Typically, a second collapse is turbulent and marked by microbubbles of water vapor [40]. Nevertheless, it is clear that the vapor also must contain permanent gases, as some bubbles, in particular, single surviving bubbles do not

show size-related fast collapse but survive for milliseconds and longer. Other microbubbles appear transiently above the main bubble.

Such microbubbles predominantly appear (i) in front of the nascent main bubble in the wake of the shock front (seen in Figure 1(a) at 3.5 μs) and (ii) in a comparable situation after bubble collapse, which also emits a shock wave. Both are explained by the heated path of the laser beam that undergoes a pressure drop after the shock front [23,48] has swept the area. The nucleation of microbubbles is eased by the pressure drop, possibly aided by pre-existing nanoparticles in the liquid. Flushing the chamber with fresh water makes the nucleation cloud more stochastic, but the phenomenon persists. Therefore, pre-existing particles enhance the microbubble cloud through either direct heating by the laser but more generally by providing nuclei for boiling at reduced pressure and elevated temperature.

This pressure drop is terminated by the increased pressure in the front of the main bubble. As result, the cloud limits are clearly defined. Figure 1(b) plots these limits as a function of delay and height above target. Sometimes these microbubbles are confused for emitted nanoparticles. Yet, nanosecond-resolved X-ray small angle scattering has refuted the existence of such fast-traveling particles [4]. On

the other hand, it has been suggested and observed earlier that hot particles may be ejected into the liquid close to the front of the nascent bubble to be excited by the laser pulse or give rise to transient bubbles when cooling down [3]. Such spots are occasionally observed, as in Figure 1 at 45 µs.

Overall, the macroscopic bubble and shock wave dynamics reproduce the established knowledge with dynamics governed by the balance of pressure, temperature, and surface tension. We do not find any signs of singular motion, such as distinct jet formation or observation of newly produced particles outside of the bubble prior to collapse. When comparing the dynamics to sophisticated numerical simulations, we assume that peculiar collapse behavior is just suppressed by the symmetry breaking of the wire target.

3.2   Atomic-scale reactions

Detection of ablated material remains challenging due to the low density and optical distortion of the bubble itself. To the best knowledge so far, the bubble is, after some microseconds have passed, uniformly filled with ejecta, such as clusters and nanoparticles [49]. These can undergo limited ripening. Keeping the phase explosion nature of the particle genesis in mind [3], these particles must exist in the earliest steps of target decomposition. Camarda et al. [50] have described the formation of metallic zinc nanoparticles, which gradually oxidized forming color centers within minutes. Other possible species are zinc peroxide (ZnO_2) [51] or zinc hydroxide ($Zn(OH)_2$) [52]. The addition of sodium dodecyl sulfate (SDS) to the aqueous ablation medium even preserved metallic zinc nanoparticles at the highest concentration [53]. This was attributed to the capping action of SDS.

Recently, we have described the detection of a substantial proportion of isolated atoms of zinc in nanosecond ablation, which react within tens of nanoseconds [27]. Corresponding X-ray absorption spectra are shown in Figure 2, with the strong prepeak at 9.662 keV being unique to a reference spectrum of zinc vapor [32]. No other compounds with such feature are observed, only organic complexes as Zn porphyrin show a weak prepeak feature [54]. This prepeak is associated with atomic resonances with multi-electron excitations and is not described in detail in the literature. Similarly strong prepeaks are found in different transition metal vapors [55-57]. While the occurrence in vapor suggests neutral atoms as a source, the resonance could also be related to ions or clusters. A shift in peak position as described below could indicate cluster formation. Yet, an *ab initio* modeling for these intermediates has not been achieved yet.

The atom content can amount up to 55% in pure water [27], a similar value to what is found here in case that reducing $NaBH_4$ is added to water. On the other hand, the oxidizing agent $HAuCl_4$ leads to a reduction of the atom contribution to 45%. The probed region was close to the interaction spot but varied by 0.2 mm in each direction, as indicated by the yellow dots in Figure 3. In the extended bubble, a lesser content is probable at larger distances above the target. Also, the atom species vanish rapidly within some 50 µs [27] similar to the present case (not shown). At the displayed delay of 22 µs in Figure 2, the prepeak has already decayed, showing some possible intermediate states with an energy-shifted prepeak, in particular for the $NaBH_4$ case. The nature of this shift remains elusive.

Still, the reaction of these early atom species results in metallic zinc nanoparticles, maybe by attachment to existing metallic particles. As can be seen in Figure 2 for both $NaBH_4$ and $HAuCl_4$, metallic particles are detected at a delay of
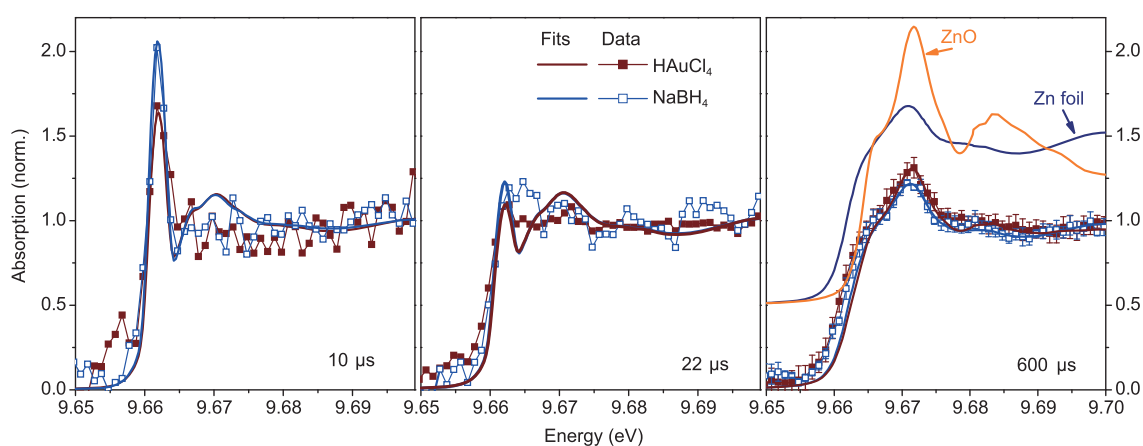

Figure 2   (Color online) Comparison of X-ray near-edge structure at different delays for the ablation runs with either $NaBH_4$ (open symbols) or $HAuCl_4$ solution (filled symbols). The bold lines show simulations of the varied amplitude of the different reference spectra to the signal (blue for $NaBH_4$ and brown for $HAuCl_4$).

600 μs as inferred from the near-edge shape. In particular, the shape of the maximum at 9.671 keV is fitted well in amplitude and position by the reference spectrum of a zinc foil. The oxide content is slightly increased for the oxidative solution (25% ± 7%), as compared with the content in the reducing environment (12%), which is seen by the slight increase in absorption at the peak's maximum at 9.671 and 9.684 keV. Thus, the oxidative action of $HAuCl_4$ is visible, but of limited significance at that short time after ablation. $HAuCl_4$ is known to be reduced even in the presence of ZnO, forming technologically relevant hybrid structures [58]. The final product of zinc ablation in a $HAuCl_4$ solution is reported to be Au@ZnO core/shell nanoparticles [59]. The observation of a similar atom content at 11 μs and oxidation at 600 μs in the case of aqueous $NaBH_4$ and pure water leads us to conclude that similar redox conditions may apply in both cases. This agrees with the observation that PLAL in water can produce an excess of gaseous hydrogen [29], in particular on non-noble metals.

This signature of permanent gases can be found in the visible stroboscopic images at delays, where all cavitation phenomena have vanished. Figure 1 shows small gas bubbles persisting at 2.5 ms after ablation. A rough estimate of the volume of these microbubbles shows that about 0.5%-1% of the initial vapor bubble may consist of permanent gases.

3.3   Distribution of ejected material

The absolute height of the absorption step at the Zn-K_α edge can serve as a measure for the total amount of ablated zinc along the X-ray beam path. To be more precise, it scales with the area density of the intersected material by the X-ray beam and can be scaled to absolute units. For a more intuitive description, we converted this density into the thickness of an equivalent film of metallic zinc that would possess the same X-ray absorption at the edge (Figure 3(c)). In a similar

fashion, the amplitude of the X-ray dark-field signal can be qualitatively related to observed particle mass (see Figure 3). The temporal behavior of the total mass at the given distances from the target shows a characteristic two-maxima modulation. This modulation has been described as being caused by a bubble that is filled with material, while the material density varies with bubble size. A simulation for a constant total material mass fits the data well. However, at the maximum bubble size, the observed mass signal is higher than calculated, which could point towards a higher density in the center of the bubble, respectively fresh material being expulsed in the center. After bubble collapse, a small fraction of the mass is left behind, in particular at a larger target distance. This could indicate limited transmission of mass through the bubble interface or viscous retraction of the ablated material in front of the bubble [3]. The retraction of the larger nanoparticles as seen in dark-field imaging (Figure 3(a)) is more complete at bubble collapse. Later on, the ablated material is dispersed into the liquid close to the target.

A total mass of 2.2×10^{-7} g per ablation pulse is derived, which relates to an ablated depth per laser shot of roughly 1 μm from a 0.2 mm crater in diameter [27]. This appears surprising, given that the typical laser extinction depth in metals ranges for some tens of nanometers. We, therefore, cross-checked this finding by applying a given number of laser pulses of 10 mJ on a fixed-size flat zinc sheet and weighing out the change in target mass. Applying 10 or 20 pulses per area with a total number varied from 100 to 1200 pulses invariably results in a removed mass of 3×10^{-7}-5.5×10^{-7} g per pulse, confirming the absolute amount of ablation detected *in situ*. Fast electron and heat conduction is able to transport the absorbed energy deeper into the zinc target and cause phase explosion and evaporation. Zinc may be an extreme case compared with other metallic targets, keeping its low melting temperature and heat of vaporization in mind. In fact, the full evaporation of this mass would take 0.39 mJ of
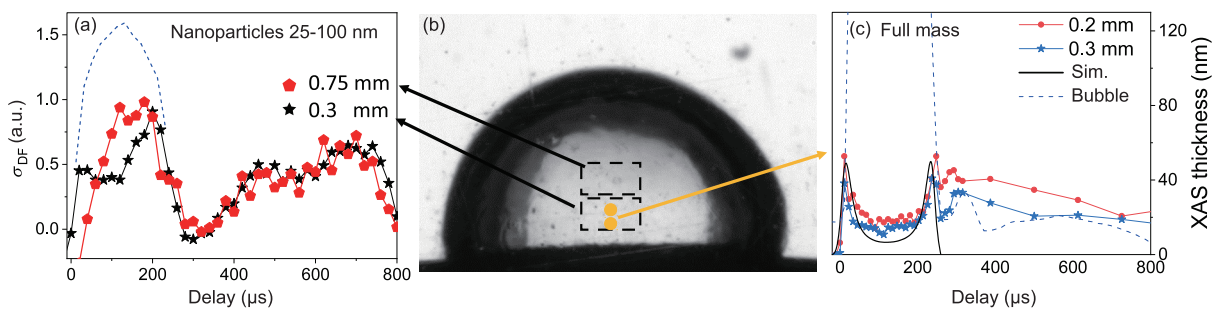

Figure 3   (Color online) Comparison of the temporal change of the dark-field signal σ_{DF} (a) related to nanoparticles and absorption amplitude at the Zn-K_α edge (c) related to the total intersected mass as equivalent (solid) Zn sheet thickness at different heights above the target. The positions (XAS, yellow dots), respectively areas (DF, dashed rectangles), where the data are derived from are shown as an overlay over a visible image snapshot (b) at 114 μs with the symbols corresponding to the traces of σ_{DF} in (a). The symbols in (a) and (b) identify the two DF regions of about 0.3 mm (black star) and 0.75 mm (red pentagon). The dashed blue lines mark the bubble dynamics.

energy. For comparison, the energy dissipated in the shock wave in water is estimated to be about 0.6 mJ from similar conditions as described in ref. [60]. The bubble energy would amount to about 1-2 mJ, which already shows that the ablation process is relatively efficient with energy lost only to residual water heating (as evidenced by the microbubble formation) and heat dissipation into the target.

3.4 Fluence threshold behavior

The partition of incident laser energy into different dissipation channels may depend on the irradiation power. Material properties may change on a sub-nanosecond time scale, which would lead to a modified deposition of energy into the target. The laser pulse length of 7 ns is long enough to further excite the nascent plasma and ejected material. Such enhanced absorption at the interface will manifest as a nonlinear reaction of the observables in PLAL [20]. We have investigated the pulse-energy dependent macroscopic ablation dynamics by continuously increasing the laser pulse energy from 0.3 to 30 mJ. Figure 4 displays the behavior of the shock front, plasma emission, and bubble growth as a function of pulse energy. The shock wave shows a deceleration behavior with distance for the impact as described earlier [48, 60, 61], starting from > 1700 m/s and decelerating after about 1 μs to a constant 1530 m/s. The steady-state shock speed is slightly higher than the speed of sound in water (1482 m/s). While the steady-state velocity does barely change with pulse energy the initial shock speed changes strongly in a range from 0.3 to 7 mJ. The intensity of the plasma emission at the same time shows a steep increase from 3 to 7 mJ. It should be noted that the plasma plume projection onto the aperture of the APM is larger than the active area. Additionally, the plasma is expected to be opaque. Therefore the increase in the intensity of light emission must be at least in part related to an increase in plasma temperature. The lifetime of the plasma is not changed strongly on a sub-microsecond time scale.

The bubble volume has earlier been reported to show a nonlinear behavior with pulse energy [20], accompanied by a corresponding increase in ablation amplitude. The maximum bubble size is shown in Figure 4(c) with a relatively large increase between 3 and 7 mJ. To collect more dense data points, the bubble has been imaged at a fixed delay after laser impact of 400 ns. The volume at this snapshot confirms the disproportionally large increase between 5 and 10 mJ. All these observations support the notion that laser localization and thus ablation efficiency is not a linear function of laser power (or fluence), but rather shows a threshold behavior in a transition region. This may be linked to enhanced absorption of laser light in the surface-near region after the first formation of expulsed material and plasma. Thus, a large amount
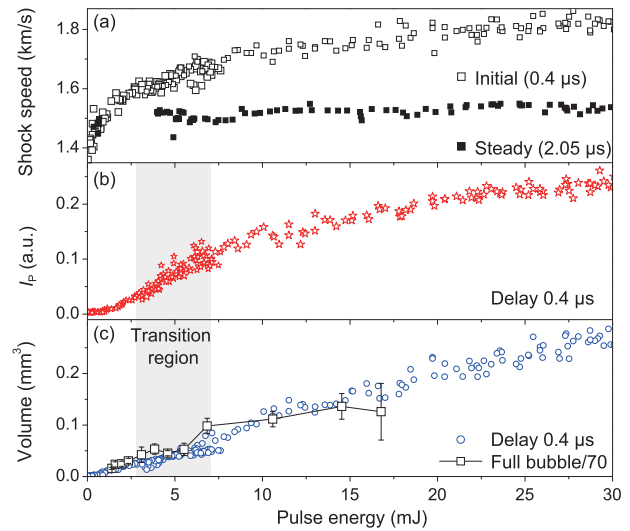

Figure 4 (Color online) Change of the shock front speed (a), plasma intensity (b), and bubble size (c) as a function of laser pulse energy. The maximum bubble size (which varies in delay) is overlaid after reduction by a factor of 70 onto the bubble size at a fixed delay of 0.4 μs. The transition region of enhanced energy localization at the interface is marked by the shaded area. Note that the typical pulse energy for X-ray spectroscopy and imaging in the present study is around 10-12 mJ.

of atomic zinc species as discussed above is explained by sustained heating of the plume and secondary atomization.

The power threshold together with the other macroscopic observations illustrates nicely that there is a preferred laser power interval for efficient ablation which ranges from 5 to 20 mJ in our case. A tighter focusing may lower the first threshold considerably but requires different optics or laser beam profiles. On the other hand, the upper threshold is defined by the more serious water heating along the laser path to initiate optical breakdown, as well as the ejection of larger particles on the microscale. There is an indication for such larger particles based on observations that a higher probability of microbubbles adjacent to the cavitation bubble is observed at above 20 mJ and the cavitation bubble surface in general gets more corrugated.

4 Summary

The interior of cavitating bubbles in pulsed ablation in liquids can be accessed by time-resolved X-ray probes in order to resolve the processes that lead to nanoparticle formation and speciation. The oxidation kinetics during ablation from a zinc wire in water is addressed by XAS. In particular, the near-edge structure provides information that the primary product formed after ablation in the bubble and after bubble collapse are zinc particles with the spectral shape of metallic zinc. Within the first few microseconds atom species

are observed as well. The high content of this species is explained by the extreme conditions in the plasma. This plasma is heated by the relatively long duration of the nanosecond laser, which could foster atomization. A variation of fluence shows a variation of ablation conditions from a low-fluence range up to 5-7 mJ with a reduced coupling of energy into shock wave, plasma, and cavitation bubble, followed by a more efficient coupling.

Speciation can be influenced by the addition of reductive or oxidative solutes, as $NaBH_4$ and $HAuCl_4$, respectively. We found nevertheless, that the additional oxidation by the aurate solute in a short time is limited. The formation of hybrid nanoparticles as desired for technological applications [62] is probably proceeding on much longer time scales, comparable to that of zinc nanoparticle oxidation within minutes in water.

The spatiotemporal distribution of ablated material can be inferred from X-ray spectroscopy and X-ray dark-field imaging, the latter being sensitive to nanoparticles from 25-100 nm in diameter. The conclusion here is that the cavitation bubble forms confinement for the ablated species, however, to a different extent. Nanoparticle retention after the first bubble collapse seems to be rather complete, while the turbulent bubble rebound on the wire results later in dispersing of nanoparticles into the liquid. The retention of the total mass does not seem to be complete. This leads to the conclusion that the bubble interface might be transmissive to smaller nanoparticles and dissolved clusters.

1   A. Fojtik, M. Giersig, and A. Henglein, Ber. Bunsengesellschaft Phys. Chem. **97**, 1493 (1993).

2   J. Neddersen, G. Chumanov, and T. M. Cotton, Appl. Spectrosc. **47**, 1959 (1993).

3   C. Y. Shih, R. Streubel, J. Heberle, A. Letzel, M. V. Shugaev, C. Wu, M. Schmidt, B. Gökce, S. Barcikowski, and L. V. Zhigilei, Nanoscale **10**, 6900 (2018).

4   S. Reich, A. Letzel, A. Menzel, N. Kretzschmar, B. Gökce, S. Barcikowski, and A. Plech, Nanoscale **11**, 6962 (2019).

5   V. Amendola, S. Scaramuzza, L. Litti, M. Meneghetti, G. Zuccolotto, A. Rosato, E. Nicolato, P. Marzola, G. Fracasso, C. Anselmi, M. Pinto, and M. Colombatti, Small **10**, 2476 (2014).

6   S. Reichenberger, G. Marzun, M. Muhler, and S. Barcikowski, ChemCatChem **11**, 4489 (2019).

7   M. E. Povarnitsyn, and T. E. Itina, Appl. Phys. A **117**, 175 (2014).

8   C. Y. Shih, C. Wu, M. V. Shugaev, and L. V. Zhigilei, J. Colloid Interface Sci. **489**, 3 (2017).

9   C. Y. Shih, M. V. Shugaev, C. Wu, and L. V. Zhigilei, Phys. Chem. Chem. Phys. **22**, 7077 (2020).

10   A. Matsumoto, A. Tamura, K. Fukami, Y. H. Ogata, and T. Sakka, J. Appl. Phys. **113**, 053302 (2013).

11   A. Matsumoto, A. Tamura, T. Honda, T. Hirota, K. Kobayashi, S. Katakura, N. Nishi, K. Amano, K. Fukami, and T. Sakka, J. Phys. Chem. C **119**, 26506 (2015).

12   J. Lam, D. Amans, F. Chaput, M. Diouf, G. Ledoux, N. Mary, K. Masenelli-Varlot, V. Motto-Ros, and C. Dujardin, Phys. Chem. Chem. Phys. **16**, 963 (2014).

13   J. Lam, D. Amans, C. Dujardin, G. Ledoux, and A. R. Allouche, J. Phys. Chem. A **119**, 8944 (2015), arXiv: 1707.08434.

14   A. Letzel, B. Gökce, P. Wagener, S. Ibrahimkutty, A. Menzel, A. Plech, and S. Barcikowski, J. Phys. Chem. C **121**, 5356 (2017).

15   A. Letzel, S. Reich, T. dos Santos Rolo, A. Kanitz, J. Hoppius, A. Rack, M. P. Olbinado, A. Ostendorf, B. Gökce, A. Plech, and S. Barcikowski, Langmuir **35**, 3038 (2019).

16   M. Takeuchi, and K. Sasaki, Appl. Phys. A **122**, 312 (2016).

17   C. Y. Shih, M. V. Shugaev, C. Wu, and L. V. Zhigilei, J. Phys. Chem. C **121**, 16549 (2017).

18   H. Oguchi, T. Sakka, and Y. H. Ogata, J. Appl. Phys. **102**, 023306 (2007).

19   D. S. Zhang, J. Liu, and C. H. Liang, Sci. China-Phys. Mech. Astron. **60**, 074201 (2017).

20   S. Reich, P. Schönfeld, A. Letzel, S. Kohsakowski, M. Olbinado, B. Gökce, S. Barcikowski, and A. Plech, ChemPhysChem **18**, 1084 (2017).

21   M. Dell'Aglio, V. Motto-Ros, F. Pelascini, I. B. Gornushkin, and A. De Giacomo, Plasma Sources Sci. Technol. **28**, 085017 (2019).

22   P. Wagener, S. Ibrahimkutty, A. Menzel, A. Plech, and S. Barcikowski, Phys. Chem. Chem. Phys. **15**, 3068 (2013).

23   S. Reich, P. Schönfeld, P. Wagener, A. Letzel, S. Ibrahimkutty, B. Gökce, S. Barcikowski, A. Menzel, T. dos Santos Rolo, and A. Plech, J. Colloid Interface Sci. **489**, 106 (2017).

24   S. Ibrahimkutty, P. Wagener, A. Menzel, A. Plech, and S. Barcikowski, Appl. Phys. Lett. **101**, 103104 (2012).

25   K. Ando, and T. Nakajima, Nanoscale **12**, 9640 (2020).

26   S. Pascarelli, O. Mathon, T. Mairs, I. Kantor, G. Agostini, C. Strohm, S. Pasternak, F. Perrin, G. Berruyer, P. Chappelet, C. Clavel, and M. C. Dominguez, J. Synchrotron Rad. **23**, 353 (2016).

27   S. Reich, J. Göttlicher, A. Ziefuss, R. Streubel, A. Letzel, A. Menzel, O. Mathon, S. Pascarelli, T. Baumbach, M. Zuber, B. Gökce, S. Barcikowski, and A. Plech, Nanoscale **12**, 14011 (2020).

28   M. R. Kalus, N. Bärsch, R. Streubel, E. Gökce, S. Barcikowski, and B. Gökce, Phys. Chem. Chem. Phys. **19**, 7112 (2017).

29   M. R. Kalus, R. Lanyumba, N. Lorenzo-Parodi, M. A. Jochmann, K. Kerpen, U. Hagemann, T. C. Schmidt, S. Barcikowski, and B. Gökce, Phys. Chem. Chem. Phys. **21**, 18636 (2019).

30   S. Reich, J. Göttlicher, A. Letzel, B. Gökce, S. Barcikowski, T. dos Santos Rolo, T. Baumbach, and A. Plech, Appl. Phys. A **124**, 71 (2018).

31   M. Borri, C. Cohen, J. Groves, W. Helsby, O. Mathon, L. McNicholl, S. Pascarelli, N. Sévelin-Radiguet, R. Torchio, and M. Zuvic, Nucl. Instrum. Methods Phys. Res. Sect. A **1017**, 165800 (2021).

32 A. Mihelič, A. Kodre, I. Arčon, J. Padežnik Gomilšek, and M. Borowski, Nucl. Instrum. Methods Phys. Res. Sect. B **196**, 194 (2002).

33 D. Zhang, B. Gökce, and S. Barcikowski, Chem. Rev. **117**, 3990 (2017).

34 S. Barcikowski, A. Plech, K. S. Suslick, and A. Vogel, MRS Bull. **44**, 382 (2019).

35 J. Long, M. Eliceiri, Z. Vangelatos, Y. Rho, L. Wang, Z. Su, X. Xie, Y. Zhang, and C. P. Grigoropoulos, Opt. Express **28**, 14300 (2020).

36 M. S. Plesset, and A. Prosperetti, Annu. Rev. Fluid Mech. **9**, 145 (1977).

37 T. Hupfeld, G. Laurens, S. Merabia, S. Barcikowski, B. Gökce, and D. Amans, J. Appl. Phys. **127**, 044306 (2020).

38 J. Lam, J. Lombard, C. Dujardin, G. Ledoux, S. Merabia, and D. Amans, Appl. Phys. Lett. **108**, 074104 (2016).

39 S. Kohsakowski, B. Gökce, R. Tanabe, P. Wagener, A. Plech, Y. Ito, and S. Barcikowski, Phys. Chem. Chem. Phys. **18**, 16585 (2016).

40 S. Reich, T. dos Santos Rolo, A. Letzel, T. Baumbach, and A. Plech, Appl. Phys. Lett. **112**, 151903 (2018).

41 Z. Zhang, A. Wang, J. Wu, Y. Z. Liu, D. Huang, Y. Qiu, and J. Li, AIP Adv. **9**, 125048 (2019).

42 M. Senegačnik, K. Kunimoto, S. Yamaguchi, K. Kimura, T. Sakka, and P. Gregorčič, Ultrason. Sonochem. **73**, 105460 (2021).

43 A. Shima, and Y. Sato, Ing. Arch. **48**, 85 (1979).

44 C. Lechner, W. Lauterborn, M. Koch, and R. Mettin, Phys. Rev. Fluids **4**, 021601(R) (2019).

45 F. Reuter, and C. D. Ohl, Appl. Phys. Lett. **118**, 134103 (2021).

46 S. Reich, A. Letzel, B. Gökce, A. Menzel, S. Barcikowski, and A. Plech, ChemPhysChem **20**, 1036 (2019).

47 N. Dabir-Moghaddam, Z. Liu, and B. Wu, J. Appl. Phys. **121**, 044908 (2017).

48 T. Tsuji, Y. Okazaki, Y. Tsuboi, and M. Tsuji, Jpn. J. Appl. Phys. **46**, 1533 (2007).

49 S. Ibrahimkutty, P. Wagener, T. S. Rolo, D. Karpov, A. Menzel, T. Baumbach, S. Barcikowski, and A. Plech, Sci. Rep. **5**, 16313 (2015).

50 P. Camarda, F. Messina, L. Vaccaro, G. Buscarino, S. Agnello, F. M. Gelardi, and M. Cannas, J. Appl. Phys. **120**, 124312 (2016).

51 M. A. Gondal, Q. A. Drmosh, Z. H. Yamani, and T. A. Saleh, Appl. Surf. Sci. **256**, 298 (2009).

52 Z. Yan, R. Bao, and D. B. Chrisey, Chem. Phys. Lett. **497**, 205 (2010).

53 H. Zeng, W. Cai, Y. Li, J. Hu, and P. Liu, J. Phys. Chem. B **109**, 18260 (2005).

54 E. Castorina, E. D. Ingall, P. L. Morton, D. A. Tavakoli, and B. Lai, J. Synchrotron Rad. **26**, 1302 (2019).

55 U. Arp, B. M. Lagutin, G. Materlik, I. D. Petrov, B. Sonntag, and V. L. Sukhorukov, J. Phys. B-At. Mol. Opt. Phys. **26**, 4381 (1993).

56 C. M. Teodorescu, J. M. Esteva, M. Womes, A. El Afif, R. C. Karnatak, A. M. Flank, and P. Lagarde, J. Electron Spectr. Relat. Phenom. **106**, 233 (2000).

57 A. Kodre, I. Arcon, J. P. Gomilsek, R. Preseren, and R. Frahm, J. Phys. B-At. Mol. Opt. Phys. **35**, 3497 (2002).

58 M. E. Aguirre, G. Perelstein, A. Feldhoff, A. Condó, A. J. Tolley, and M. A. Grela, New J. Chem. **39**, 909 (2015).

59 A. M. Mostafa, and E. A. Mwafy, J. Mater. Res. Tech. **9**, 3241 (2020).

60 A. Vogel, S. Busch, and U. Parlitz, J. Acoust. Soc. Am. **100**, 148 (1996).

61 A. Chemin, M. W. Fawaz, and D. Amans, Appl. Surf. Sci. **574**, 151592 (2022).

62 H. Zhang, S. Wu, J. Liu, Y. Cai, and C. Liang, Phys. Chem. Chem. Phys. **18**, 22503 (2016).